Scripta Materialia 164 (2019) 42–47

Contents lists available at ScienceDirect

Scripta Materialia

journal homepage: www.elsevier.com/locate/scriptamat

Immiscible nanostructured copper-aluminum-niobium alloy with excellent precipitation strengthening upon friction stir processing and aging

Subhasis Sinha [a], Mageshwari Komarasamy [a], Saket Thapliyal [a], Bharat Gwalani [a], Shivakant Shukla [a], Kristopher A. Darling [b], Rajiv S. Mishra [a,*]

[a] Center for Friction Stir Processing, Department of Materials Science and Engineering, Advanced Materials and Manufacturing Processes Institute, University of North Texas, Denton, TX 76207, USA
[b] Army Research Laboratory, Weapons and Materials Research Directorate, APG, MD 21005, USA

A R T I C L E I N F O

Article history:
Received 22 October 2018
Received in revised form 11 January 2019
Accepted 22 January 2019
Available online xxxx

Keywords:
Friction stir processing
Copper alloys
Nanocrystalline microstructure
Precipitation
Hardness

A B S T R A C T

A ternary immiscible nanostructured Cu-Al-Nb alloy was fabricated by friction stir processing of mechanically compacted pellets. Subsequently, aging was carried out at 563 K for various times. The material exhibited hardness of ~4.3 ± 0.1 GPa in the peak-aged condition (aging for 6 h), which is remarkable among Cu-based ternary immiscible alloys. The excellent strength of the material is attributed to Hall-Petch strengthening due to the extremely refined nanocrystalline structure, coupled with precipitation strengthening due to a uniform distribution of nano-scale Al- and Nb-rich precipitates or clusters, as confirmed by X-ray diffraction and microstructural characterization.

Nanocrystalline materials provide excellent strengthening through grain refinement; however, to stabilize the nanocrystalline grains, grain growth must be inhibited. This may be achieved through grain boundary pinning by solutes and particles [1,2]. Darling et al. [3] described a Cu-Ta immiscible nanocrystalline alloy where nanoclusters of atoms or nano-precipitates effectively pin the grain boundaries, with resulting excellent strength and creep resistance, along with mechanical and thermal stability.

Over the years, alloying of immiscible elements has generated considerable interest [4–12]. Ma [7] stated that the non-equilibrium structures formed in these alloys offer advantageous possibilities such as tailored magnetic response in a usually immiscible mixture of elements or thermal decomposition of the alloy by ion irradiation to form patterns. Among the various techniques for fabricating immiscible nanostructured alloys [13–20], friction stir processing (FSP) [21] is a relatively new route to produce ternary immiscible alloys like Cu-Ag-Nb [22].

The present study describes a ternary immiscible alloy containing copper, aluminum and niobium, henceforth referred to as a Cu-Al-Nb system. Some earlier researchers studied Cu-Al-Nb alloys [23] and their shape memory behavior [24,25]. The present study aims to: (1) study the evolution of this ternary immiscible alloy by FSP; (2) explain the strengthening mechanisms; and (3) elaborate on how Al and Nb contribute to the underlying mechanisms.

Cylindrical pellets of Cu-Al-Nb were made from Cu-10 wt% Al ($Cu_{80}Al_{20}$ in at.%) powder (1–20 μm) and Nb powder (1–5 μm) by compaction using a hydraulic press. Calculated weights of the Cu – 10 wt% Al and Nb powders (in the desired ratios) were weighed out using a Scout Pro laboratory weighing machine (with up to 200 g capacity) to obtain a mixture with total weight of 700 g. Then the container with the mixed powder was put on rollers for 24 h to facilitate thorough and uniform mixing throughout. The amounts of powders used were calculated to obtain a stoichiometry (in at.%) of $Cu_{76}Al_{20}Nb_4$. The pellets were ~10 mm in diameter and 4 mm in height. Each Cu-Al-Nb pellet was placed in a hole in a high-purity Cu block. The holes were machined using a mini computer numerical control (CNC) machine to precisely fit the respective pellets. FSP was then carried out using a H13 steel tool with pin height of 2.3 mm, pin diameter at the root and tip of 6 mm and 3.75 mm, respectively; and shoulder diameter of 12 mm. The tool had a conical pin with step-spiral profile and concave shoulder. The plunge depth was 2.5 mm, and stirring was carried out at 600 rotations per minute (rpm) for a dwell time of 120 s. Position control was used during the dwelling in FSP. The as-FSP specimens were subjected to aging at 290 °C (563 K) for 30 min, 1 h, 2 h, 4 h, 6 h and 8 h.

Hardness of the as-FSP and aged specimens was measured with a Vickers indenter using 500 g load with 10 s dwell time. Vickers hardness measurements were performed at various locations (with respect to the

* Corresponding author.
E-mail address: Rajiv.Mishra@unt.edu (R.S. Mishra).

https://doi.org/10.1016/j.scriptamat.2019.01.038
1359-6462/

depth within the processed volume) and on multiple processed pellets. Based on the variation in hardness at different locations, a selected location (with respect to the depth within the processed volume) approximately 50 μm below the tool pin tip was analyzed for comparison. For the aged specimens, hardness was measured only at this location. For the selected location (in terms of depth beneath the surface), 8–10 Vickers hardness measurements were taken for each condition.

X-ray diffraction (XRD) of as-FSP and aged specimens was carried out using a Rigaku Ultima III diffractometer operating at 40 kV and 44 mA. Microstructural characterization of the as-FSP and aged specimens was done using FEI Nova NanoSEM 230 for backscatter electron (BSE) imaging. Corresponding EDS (electron dispersive spectroscopy) compositional mapping was performed using TEAM™ software. Transmission electron microscopy (TEM) specimen of peak-aged specimen was prepared by Focused Ion Beam (FIB) milling process using FEI Nova 200 NanoLab Dual Beam FIB/FESEM. TEM characterization including scanning TEM (STEM) compositional analysis was carried out using a FEI Tecnai G2 F20 S-Twin 200 keV field emission STEM.

The BSE image of the transverse section of the as-processed specimen clearly depicts the lack of coarse Nb particles in the processed volume (Fig. 1(a)); whereas the unprocessed volume shows several coarse Nb particles, as confirmed by the corresponding EDS elemental map for Nb (Fig. 1(b1)). The processed volume also contains finer Nb-rich particles that are visible at a slightly higher magnification (Fig. 1(b2)). The high magnification BSE image in Fig. 1(c) shows a distribution of nano-scale precipitates in the processed volume. ImageJ software was used to calculate precipitate size and distribution. The number density of precipitates was 34/μm^2, and the average size of the precipitates was 23 nm. The EDS maps in Fig. 1(d–f) show that Nb is also distributed uniformly in the matrix (Fig. 1(f)). Cu and Al are uniformly present in the matrix (Fig. 1(d and e)) because Cu-10 wt% Al ($Cu_{80}Al_{20}$ in at.%) powder was used as the starting material. However, Nb dispersal throughout the matrix (Fig. 1(f)) in addition to the fine particles observed in Fig. 1(b2) suggests that plastic strain and temperature during FSP caused fragmentation of the large, unmixed Nb particles and facilitated sufficient mixing of the Nb with Cu-Al present in the matrix. The

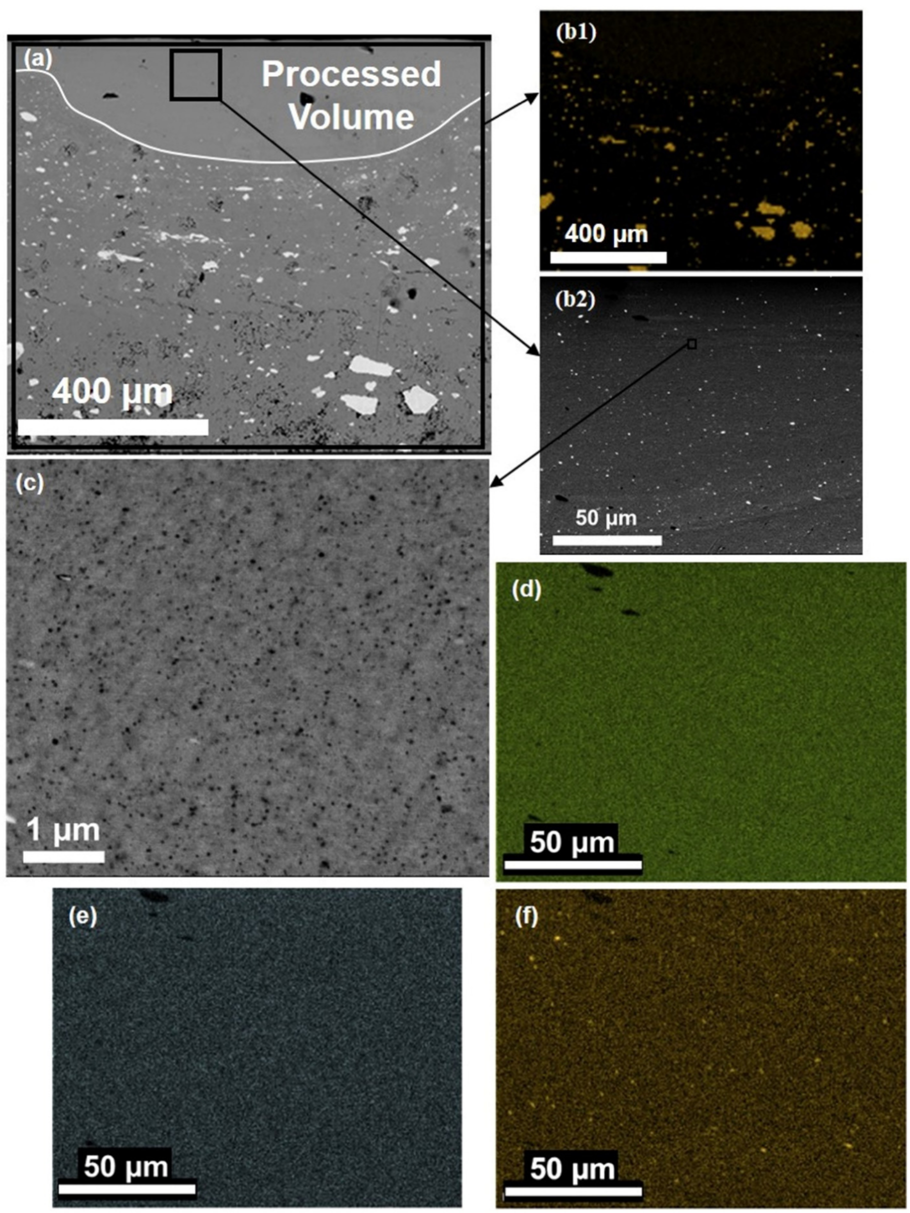

Fig. 1. Microstructure after FSP. (a) BSE image of the transverse section, (b1) EDS elemental map for Nb of region shown in (a), (b2) BSE image of region within the processed volume, (c) high magnification BSE image of the processed region, and (d–f) EDS elemental maps for region shown in (b2) for (d) Cu (e) Al and (f) Nb.

shear mixing mechanisms during FSP were discussed earlier [22]. The uniform distribution of all three elements throughout the processed volume means that Cu, Al and Nb atoms can combine to form clusters without having to move large distances; that is, the combination of these elements is not severely restricted by their diffusivity or mobility. FSP leads to a non-equilibrium condition that facilitates the mixing of Cu and Al with Nb atoms in the vicinity through multiple operative mechanisms. The possible shear mixing mechanisms include dislocations crossing the interface, shear-controlled atomic shuffling as well as localized diffusion. All these mechanisms enable the combination of Cu and Al atoms with Nb atoms to form a distribution of fine precipitates or clusters in the as-FSP microstructure.

Previous welding studies utilizing iterative mesh-based hardness mapping showed that hardness is sensitive to location within the weld [26]. Hence, spatial measurements of hardness were performed on the as-FSP specimen to obtain the spread in hardness across the processed region and the variation of hardness with depth below the tool tip. These results are shown in Fig. 2. Hardness decreases with depth from the top of the processed region (along the black, red, blue and green lines). The spread in hardness horizontally across the processed volume (along the yellow line at the top of the processed volume) is lower, except near the shear zone adjacent to the tool shoulder. Thus, hardness distribution is uniform at a particular depth, but varies with depth beneath the tool tip. Therefore, a particular location roughly 50 μm beneath the tool pin tip was selected for all comparison in the present study.

The variation of hardness in the as-FSP condition and after aging for various lengths of time is shown in Fig. 3(a). Hardness of the as-FSP specimen is ~3.9 ± 0.2 GPa. Hardness increased with aging time up to 6 h, reaching peak hardness of ~4.3 ± 0.1 GPa; while in the overaged condition (8 h), hardness decreased to ~4 ± 0.1 GPa. The hardness of nanocrystalline Cu with grain size of the order of tens of nm (<100 nm) is ~2.5 GPa [27,28], which gives an idea about the Hall-Petch strengthening contribution. Therefore, the remarkable hardness (>4 GPa) of the present material after processing and aging is attributed to the combined effect of Hall-Petch strengthening and nano-scale precipitation strengthening.

The XRD pattern of the peak-aged specimen is shown in Fig. 3(b). Overlapping peaks for Cu and Al-Nb rich phases ($AlNb_3$ or Al_3Nb) are observed. The presence of $AlNb_3$ and Al_3Nb peaks indicates that Al-Nb rich precipitates or clusters are formed in the material. The small Nb peaks suggest that some Nb remained as particles that did not go into solid solution with the matrix. However, the Nb peaks may be due partly to a signal from the unprocessed volume in the specimen.

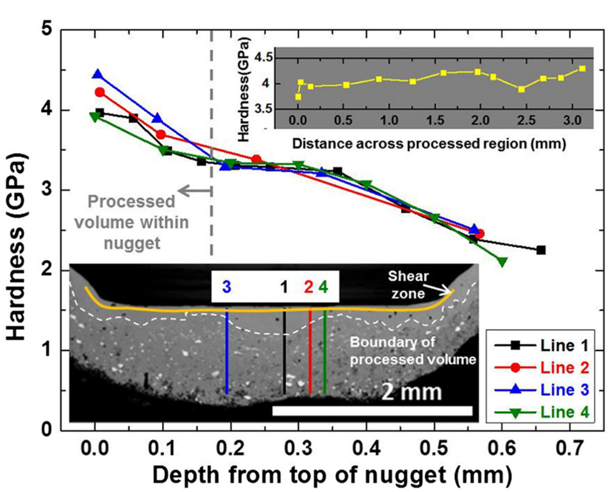

Fig. 2. Spatial variation of hardness in the processed region of as-FSP specimen. (For interpretation of the references to colour in this figure, the reader is referred to the web version of this article.)

Fig. 3(c) shows BSE image of the peak-aged (6 h) specimen. A distribution of fine precipitates throughout the matrix is observed, similar to the as-FSP microstructure (Fig. 1(c)). However, aging increased the average size of precipitates from 23 to 34 nm; while number density decreased from 34 to 24/μm^2, indicating a slight increase in spacing between the precipitates. In precipitation-hardened alloys, precipitate size increases with increase in aging time, with corresponding increase in strength up to the peak aged condition. In the overaged condition, the precipitates coarsen further but result in decrease in strength due to the effect of increase in inter-particle spacing [29]. Although the number density of precipitates for the present as-FSP and peak-aged specimens obtained from BSE images is probably an underestimate, however, it gives some idea about the change in precipitate distribution. Hardness increases by ~441 MPa from the as-FSP to peak aged (6 h) condition, after which it decreases by ~363 MPa from the peak aged (6 h) to the overaged (8 h) condition. This indicates that the precipitates reach optimum size in the peak aged (6 h) condition, but further aging to 8 h causes weakening due to increase in spacing between precipitates.

The bright field (BF) TEM image of the peak-aged specimen is shown with corresponding diffraction pattern (DP) in the inset in Fig. 3(d). Indexing of polycrystalline ring pattern (Fig. 3(e)) confirms face centered cubic (f.c.c.) crystal structure. Apart from the dark contrast nano-precipitates seen in the BSE image (Fig. 3(c)), some high-Z bright contrast nano-precipitates are also seen (typical example highlighted by yellow dotted line in Fig. 3(d)). Convergent beam micro-diffraction patterns from [111] and [112] f.c.c. zone axes are shown in Fig. 3 (f) and (g), respectively. The extra spots (highlighted by yellow circles apart from the fundamental f.c.c. spots) also suggest the presence of additional nano-precipitates in the f.c.c. matrix. This will be confirmed in further STEM analysis. Also, it is clear from Fig. 3(d) that the matrix consists of fine nanocrystalline grains. The grain size is of the order of tens of nm, which is the source of the Hall-Petch contribution to material strength. A few nano-scale twins are also observed, as highlighted by the yellow arrows in Fig. 3(d).

Imaging in high angle-annular dark field (HAADF) STEM mode and compositional analysis by EDS was carried out on the peak aged (6 h) specimen to study the nano-scale structure in greater detail, as shown in Fig. 4(a) and (b). Deformation and annealing twins (insets in Fig. 4 (a)) are revealed. The deformation twins are distinguished from annealing twins by the more lenticular shape of the former [30]. The presence of the deformation twins suggests that few nano-scale twins were nucleated during the FSP process to accommodate strain.

The compositional analysis reveals various phases, referred to as Light Grey, Dark Grey, White and Black in Fig. 4. The Light Grey phase is Nb-rich while the Dark Grey phase is Nb-deficient and seems to form along grain boundaries. In addition, White Nb-rich and Black Al-rich precipitates are found, whose size is of the order of tens of nm. STEM imaging also suggests further decomposition within the phases, as illustrated for the Black Al-rich phase in the inset in Fig. 4(b). Overall, a microstructural analysis reveals that the excellent strength of the material is attributed to the combination of Hall-Petch and precipitation strengthening.

Table 1 presents a theoretical estimate of the amount of Al and Nb in the starting raw material mixture used to make the pellets (prior to mechanical compaction) and the corresponding amounts that may be consumed to form $AlNb_3$ or Al_3Nb precipitates. The amounts are calculated based on a total of 700 g of the powder mixture. The calculations indicate that if all Nb combines with Al to form $AlNb_3$ precipitates, 4.1 g of Al is consumed out of the initial 65.1 g in the mixture. The corresponding amount for the formation of Al_3Nb is 36.6 g Al consumed. In the previous STEM compositional analysis, the Al-content in all the specific phases shown was greater than the original Al-content of the starting material (20 at.% Al). This implies that the phase list revealed in STEM analysis is also not exhaustive and there may be Al-depleted regions which were not captured. Therefore, Al-content in the matrix was also estimated from the peak shift of the Cu peaks in XRD pattern of peak-

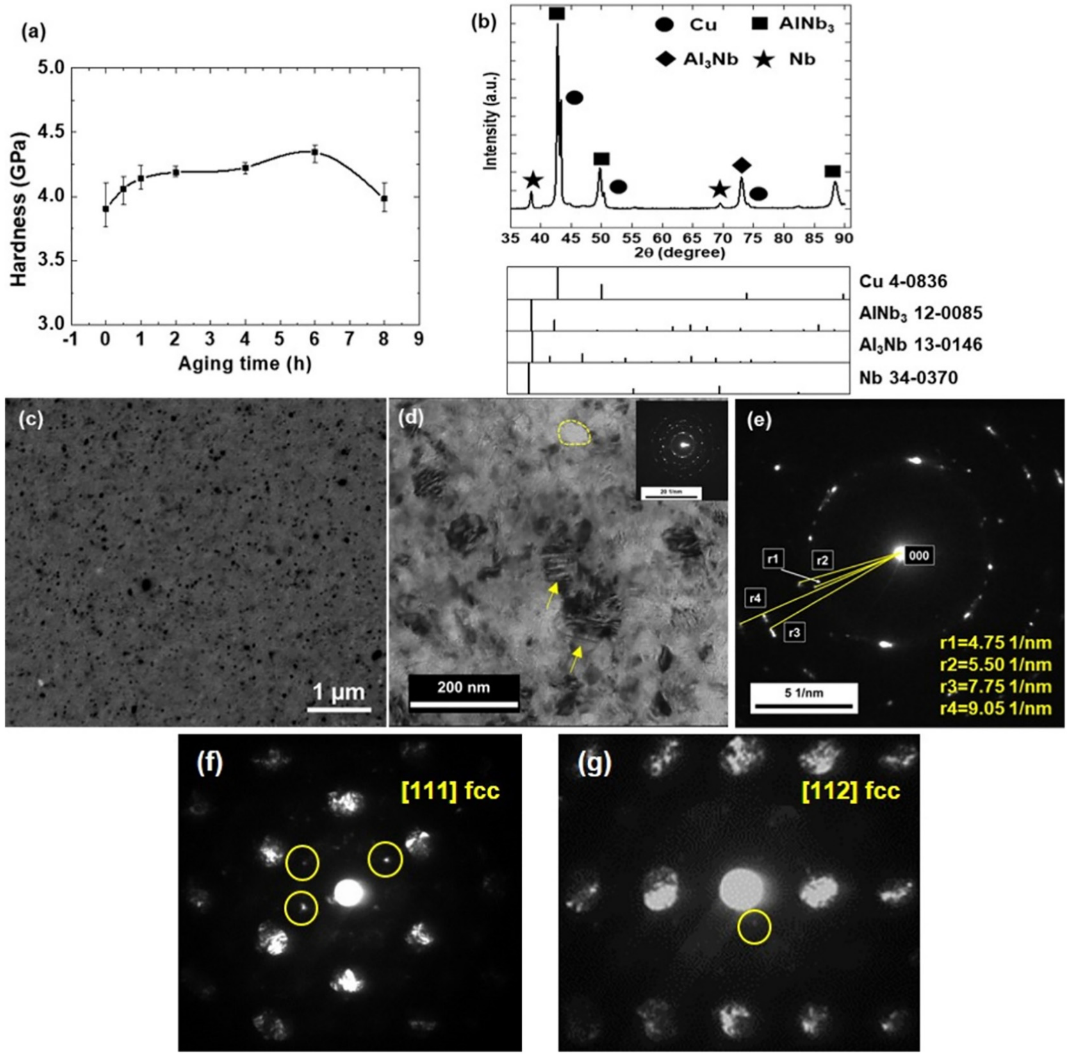

Fig. 3. (a) Hardness response of Cu-Al-Nb FSP specimens as a function of aging time, (b) XRD pattern of the peak-aged specimen with standard lines for various phases, (c) BSE image showing distribution of precipitates in peak-aged sample, (d) TEM bright field (BF) image showing microstructure of peak-aged sample (e) TEM diffraction pattern (DP), (f) convergent beam micro-diffraction pattern for $[111]_{fcc}$ zone axis and (g) $[112]_{fcc}$ zone axis. (For interpretation of the references to colour in this figure, the reader is referred to the web version of this article.)

aged specimen (Fig. 3(b)), as shown in Table 2. The lattice constant of the Cu-Al matrix after precipitation was 3.6176 Å. The variation of lattice constant with concentration for Cu-Al is reported by Lubarda [31]. Accordingly, the amount of Al in the matrix is ~4 at.%. This means that for 700 g total powder starting mixture, 24.7 g of Al remained in the matrix (out of the initial 65.1 g), while 40.4 g was consumed. Since lower Al

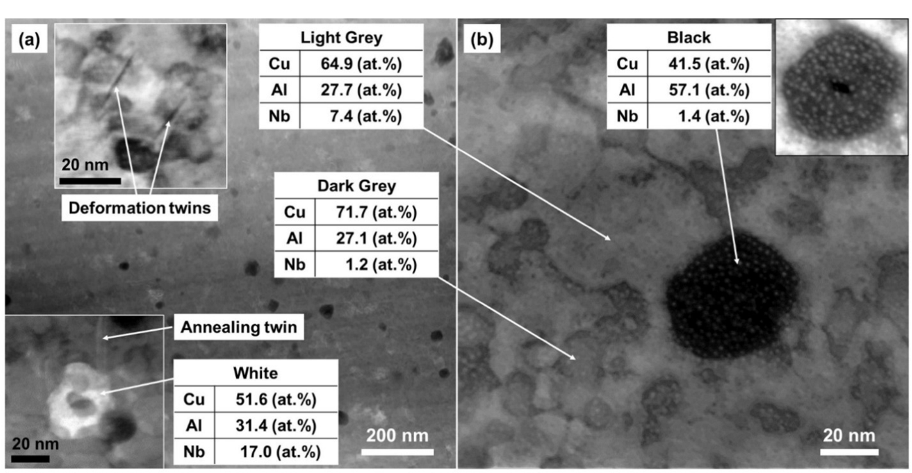

Fig. 4. STEM images of peak-aged Cu-Al-Nb sample at (a) low magnification and (b) high magnification with compositional analysis and various features highlighted as insets.

Table 1
Theoretical calculations for formation of Al-Nb precipitates.

Stoichiometry of the Cu-Al-Nb powder (at.%)	$Cu_{76}Al_{20}Nb_4$
Amount of $Cu_{80}Al_{20}$ in 700 g total powder (g)	657.9
Amount of Nb in 700 g initial mixture	42.1
Amount of Cu present in 700 g initial mixture	592.8
Amount of Al in 700 g initial mixture (g)	65.1
Al consumed if all Nb forms $AlNb_3$ (g)	4.1
Al consumed if all Nb forms Al_3Nb (g)	36.6

remained in the matrix than expected from Table 1, clearly, additional non-stoichiometric clusters of Cu, Al and Nb are formed or some of the Al may have formed oxide phase which is not detected in the XRD pattern. This is also consistent with the STEM compositional analysis that indicated the formation of various Al- and Nb-rich phases, suggesting further decomposition within phases.

The possible mechanism of formation of the Al- and Nb-rich clusters or precipitates is that Nb enters the matrix to combine with Cu and Al, which would involve atomic level mixing by mechanically driven dissolution [4,16,32,33]. Since FSP leads to considerable fragmentation of the Nb particles, upon reduction to nano-scale clusters, Nb atoms may diffuse into the matrix to undergo atomic level mixing. FSP causes fragmentation of Nb particles, thereby increasing the interface area between Nb particles and the Cu-Al matrix. The increased interface area facilitates forced shear mixing wherein Cu dislocations with Al atoms present in them are forced across the interface into the Nb lattice.

While Hall-Petch and precipitation hardening are the main strengthening mechanisms, a few nano-scale deformation twins were also observed. Nanotwinning in pure nanocrystalline Cu is well-known [34-38]; however, these nano-scale growth twins are formed by specific fabrication techniques like pulsed electrodeposition or magnetron sputtering. On the other hand, deformation twinning in Cu-Al alloys depends on Al in solid solution, which reduces the stacking fault energy (SFE) of Cu [39-41]. Cu − 10 at.% Al alloy was reported to deform only by deformation twinning [42]. Therefore, the nucleation of a few deformation twins in the present case is due to the presence of Al in solid solution with Cu, which reduces the SFE.

Fig. 5 presents a comparison of the hardness obtained in the present Cu-Al-Nb alloy with various Cu-based immiscible alloys reported earlier [22,43,44]. Previously, Lelatko and Morawiec [24] reported hardness of Cu-Al-Nb shape memory alloys containing Ni, Co and Cr, prepared by induction melting of pure metals. They studied 3 alloys and the hardness obtained was around 250 MPa. The present friction stir processed Cu-Al-Nb alloy shows high hardness among Cu-based ternary immiscible alloys. Although higher hardness (around 5 GPa) is obtained in Cu-Nb binary immiscible alloys depending on Nb content [14,45,46], annealing causes decrease in hardness from the as-milled condition. In comparison, ternary alloys containing Ag or Al in addition to Cu and Nb (and processed by FSP) show increase in hardness after annealing. However, the as-FSP hardness and relative increase in hardness after aging are different in Cu-Ag-Nb and Cu-Al-Nb; thus, the effect of Al is different from that of Ag. Since Ag is mutually immiscible with both Cu and Nb, after forced mixing, low temperature heat treatment brings out Ag in the form of precipitates, and the same happens for Nb. Evolution of the Ag and Nb precipitates during aging contributes significantly to alloy strengthening. On the other hand, Al has good solubility in Cu and it forms intermetallics with Nb. Some Nb would react with Al during FSP and therefore, not be available for further reaction during aging. So, the increase in precipitation strengthening during aging is limited.

Table 2
Experimental estimate of Al content of matrix from XRD peak shift.

Ideal Cu peak positions (2θ, degree)	Ideal lattice constant for Cu (Å)	Observed Cu peak positions (2θ, degree)	Calculated lattice constant from peak shift (Å)	Estimated Al content in matrix (at. %)
43.297	3.6158	43.3	3.6176	4%
50.434		50.4		
74.132		74.05		

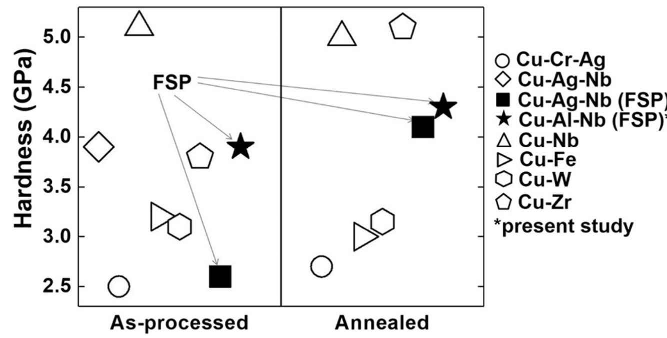

Fig. 5. Comparison of hardness of the present Cu-Al-Nb alloy with various binary and ternary Cu-based immiscible alloys reported in literature (hardness data taken from [22,43,44]).

In summary, a ternary immiscible nanostructured Cu-Al-Nb alloy was fabricated via FSP of mechanically compacted pellets. The as-FSP material exhibited hardness of 3.9 ± 0.2 GPa and after subsequent aging at 563 K, hardness of 4.3 ± 0.1 GPa was obtained in the peak aged (6 h) condition. Microstructural analysis shows extremely refined nanocrystalline grain structure containing a uniform distribution of Al- and Nb-rich nano-scale precipitates. FSP causes fragmentation of Nb particles and induces forced mixing of Cu and Al in the matrix with Nb by multiple mechanisms like dislocations crossing the interface, shear assisted atomic shuffle and diffusion, all of which lead to the formation of Al- and Nb-rich precipitates or clusters, and increase strength after aging. The excellent strength of the material is attributed to a combination of Hall-Petch strengthening and precipitation hardening.

Acknowledgments

The work was performed under a cooperative agreement between the Army Research Laboratory and the University of North Texas (W911NF-13-2-0018). Materials Research Facility (MRF) at University of North Texas is acknowledged for providing access to the microscopy facilities. The authors also acknowledge Tianhao Wang and Jonathan Jacobson for helping with using FSP and CNC machines.

References

[1] A. Michels, C.E. Krill, H. Ehrhardt, R. Birringer, D.T. Wu, Acta Mater. 47 (1999) 2143–2152.
[2] L. Shaw, H. Luo, J. Villegas, D. Miracle, Acta Mater. 51 (2003) 2647–2663.
[3] K.A. Darling, M. Rajagopalan, M. Komarasamy, M.A. Bhatia, B.C. Hornbuckle, R.S. Mishra, K.N. Solanki, Nature 537 (2016) 378–381.
[4] A.R. Yavari, P.J. Desré, T. Benameur, Phys. Rev. Lett. 68 (1992) 2235–2238.
[5] K. Sumiyama, K. Nishi, M. Shiga, M. Sakurai, K. Suzuki, J. Non-Cryst. Solids 150 (1992) 391–395.
[6] Z. Fan, S. Ji, J. Zhang, Mater. Sci. Technol. 17 (2001) 837–842.
[7] E. Ma, Prog. Mater. Sci. 50 (2005) 413–509.
[8] R. Banerjee, S. Bose, A. Genc, P. Ayyub, J. Appl. Physics 103 (033511) (2008) 1–7.
[9] H.R. Kotadia, A. Das, E. Doernberg, R. Schmid-Fetzer, Mater. Chem. Phys. 131 (2011) 241–249.
[10] A. Bachmaier, E. Neubauer, M. Kitzmantel, R. Pippan, C. Motz, IOP Conf. Ser. Mater. Sci. Eng. 63 (012023) (2014) 1–8.
[11] S.N. Arshad, T.G. Lach, J. Ivanisenko, D. Setman, P. Bellon, S.J. Dillon, R.S. Averback, J. Mater. Res. 30 (2015) 1943–1956.
[12] K. Chu, W. Zhu, C. Zhao, F. Ren, Mater. Lett. 207 (2017) 141–144.
[13] E. Ma, J.-H. He, P.J. Schilling, Phys. Rev. B 55 (1997) 5542–5545.
[14] E. Botcharova, J. Freudenberger, L. Schultz, Acta Mater. 54 (2006) 3333–3341.
[15] S. Sheibani, S. Heshmati-Manesh, A. Ataie, J. Alloys Compd. 495 (2010) 59–62.
[16] N.Q. Vo, S.W. Chee, D. Schwen, X. Zhang, P. Bellon, R.S. Averback, Scr. Mater. 63 (2010) 929–932.
[17] T. Frolov, K.A. Darling, L.J. Kecskes, Y. Mishin, Acta Mater. 60 (2012) 2158–2168.
[18] M.A. Atwater, D. Roy, K.A. Darling, B.G. Butler, R.O. Scattergood, C.C. Koch, Mater. Sci. Eng. A 558 (2012) 226–233.
[19] M.A. Atwater, R.O. Scattergood, C.C. Koch, Mater. Sci. Eng. A 559 (2013) 250–256.

[20] K.A. Darling, M.A. Tschopp, R.K. Guduru, W.H. Yin, Q. Wei, L.J. Kecskes, Acta Mater. 76 (2014) 168–185.
[21] R.S. Mishra, Z.Y. Ma, Mater. Sci. Eng. R 50 (2005) 1–78.
[22] M. Komarasamy, R.S. Mishra, S. Mukherjee, M.L. Young, JOM 67 (2015) 2820–2827.
[23] R. Schmid-Fetzer, in: G. Effenberg, S. Ilyenko (Eds.), Light Metal Systems. Part 2. Landolt-Börnstein - Group IV Physical Chemistry (Numerical Data and Functional Relationships in Science and Technology), vol. 11A2, Springer, Berlin, Heidelberg 2005, pp. 98–103.
[24] J. Lelatko, H. Morawiec, J. Phys. IV France 11 (2001) 487–492.
[25] M.C.A. da Silva, S.J.G. de Lima, Mater. Res. 8 (2005) 169–172.
[26] W.J. Brayshaw, M.J. Roy, T. Sun, V. Akrivos, A.H. Sherry, Sci. Technol. Weld. Join. 22 (2017) 404–411.
[27] M.C. Yang, F. Ye, X.C. Sun, X.K. Sun, W.D. Wei, Nanostruct. Mater. 9 (1997) 481–484.
[28] K.S. Siow, A.A.O. Tay, P. Oruganti, Mater. Sci. Technol. 20 (2004) 285–294.
[29] A.J. Kulkarni, K. Krishnamurthy, S.P. Deshmukh, R.S. Mishra, J. Mater. Res. 19 (2004) 2765–2773.
[30] W.F. Hosford, The Mechanics of Crystals and Textured Polycrystals, Oxford University Press, New York, 1993 163–184.
[31] V.A. Lubarda, Mech. Mater. 35 (2003) 53–68.
[32] G.A. Dorofeev, E.P. Elsukov, A.L. Ul'yanov, Inorg. Mater. 40 (2004) 690–699.
[33] E.P. Yelsukov, G.A. Dorofeev, A.L. Ulyanov, A.N. Maratkanova, Chem. Sustain. Dev. 13 (2005) 191–196.
[34] L. Lu, Y. Shen, X. Chen, L. Qian, K. Lu, Science 304 (2004) 422–426.
[35] X. Zhang, A. Misra, H. Wang, T.D. Shen, M. Natasi, T.E. Mitchell, J.P. Hirth, R.G. Hoagland, J.D. Embury, Acta Mater. 52 (2004) 995–1002.
[36] Y.F. Shen, L. Lu, Q.H. Lu, Z.H. Jin, K. Lu, Scr. Mater. 52 (2005) 989–994.
[37] L. Lu, R. Schwaiger, Z.W. Shan, M. Dao, K. Lu, S. Suresh, Acta Mater. 53 (2005) 2169–2179.
[38] L. Lu, X. Chen, X. Huang, K. Lu, Science 323 (2009) 607–610.
[39] P.C.J. Gallagher, Met. Trans. 1 (1970) 2429–2461.
[40] A. Rohatgi, K.S. Vecchio, G.T. Gray III, Metall. Mater. Trans. A 32A (2001) 135–145.
[41] X.-Y. San, X.-G. Liang, L.-P. Cheng, L. Shen, X.-K. Zhu, Trans. Nonferrous Metals Soc. China 22 (2012) 819–824.
[42] S.K. Varma, V. Caballero, J. Ponce, A. De La Cruz, D. Salas, J. Mater. Sci. 31 (1996) 5623–5630.
[43] D. Raabe, D. Mattissen, Acta Mater. 46 (1998) 5973–5984.
[44] D. Raabe, K. Miyake, H. Takahara, Mater. Sci. Eng. A 291 (2000) 186–197.
[45] S. Mula, H. Bahmanpour, S. Mal, P.C. Kang, M. Atwater, W. Jian, R.O. Scattergood, C.C. Koch, Mater. Sci. Eng. A 539 (2012) 330–336.
[46] S. Özerinç, K. Tai, N.Q. Vo, P. Bellon, R.S. Averback, W.P. King, Scr. Mater. 67 (2012) 720–723.